Supplementary information for "Spectroscopy of spin-split Andreev levels in a quantum dot with superconducting leads"

Arno Bargerbos,[1, *] Marta Pita-Vidal,[1, *] Rok Žitko,[2, 3] Lukas J. Splitthoff,[1]
Lukas Grünhaupt,[1] Jaap J. Wesdorp,[1] Yu Liu,[4] Leo P. Kouwenhoven,[1] Ramón
Aguado,[5] Christian Kraglund Andersen,[1] Angela Kou,[6] and Bernard van Heck[7]

[1] *QuTech and Kavli Institute of Nanoscience, Delft University of Technology, 2600 GA Delft, The Netherlands*
[2] *Jožef Stefan Institute, Jamova 39, SI-1000 Ljubljana, Slovenia*
[3] *Faculty of Mathematics and Physics, University of Ljubljana, Jadranska 19, SI-1000 Ljubljana, Slovenia*
[4] *Center for Quantum Devices, Niels Bohr Institute,*
University of Copenhagen, 2100 Copenhagen, Denmark
[5] *Instituto de Ciencia de Materiales de Madrid (ICMM),*
Consejo Superior de Investigaciones Científicas (CSIC),
Sor Juana Ines de la Cruz 3, 28049 Madrid, Spain
[6] *Department of Physics and Frederick Seitz Materials Research Laboratory,*
University of Illinois Urbana-Champaign, Urbana, IL 61801, USA
[7] *Leiden Institute of Physics, Leiden University, Niels Bohrweg 2, 2333 CA Leiden, The Netherlands*
(Dated: January 4, 2023)

CONTENTS

I. AUTHOR CONTRIBUTIONS

A.B., M.P.V., A.K. and B.v.H. conceived the experiment. Y.L. developed and provided the nanowire materials. A.B., M.P.V., L.J.S., L.G. and J.J.W prepared the experimental setup and data acquisition tools. L.J.S. deposited the

---

*These two authors contributed equally.

II. THEORY

To solidify our understanding of the results and of the mechanisms that govern the size of the spin splitting, we set up a minimal model that is able to reproduce the qualitative features observed experimentally. Our starting point is an extension of the single-impurity Anderson model (SIAM) for a quantum dot (QD) attached to two superconducting leads [1, 2], see Fig. S1. Compared to the standard SIAM, our model also contains spin-flip tunneling between the impurity and the leads due to the presence of spin-orbit coupling, as well as an additional direct tunneling term between the leads. The non-interacting part of the Hamiltonian is

$$
\begin{aligned}
H_0 = &\sum_{\sigma} \epsilon d_{\sigma}^{\dagger} d_{\sigma} + E_x S_x + E_y S_y + E_z S_z \\
&+ \sum_{i,k\sigma} \epsilon_k c_{i,k\sigma}^{\dagger} c_{i,k\sigma} + \sum_{i,k} \Delta_i \left(e^{i\phi_i} c_{i,k\uparrow}^{\dagger} c_{i,k\downarrow}^{\dagger} + \text{H.c.} \right) \\
&+ \sum_{i,k\sigma} \left(V_{i,k} c_{i,k\sigma}^{\dagger} d_{\sigma} + \text{H.c.} \right) + \sum_{i,k\sigma} \left(i W_{i,k} c_{i,k\sigma}^{\dagger} d_{\bar{\sigma}} + \text{H.c.} \right) \\
&+ \sum_{k,k',\sigma} \left(t c_{L,k\sigma}^{\dagger} c_{R,k'\sigma} + \text{H.c.} \right).
\end{aligned}
\tag{S1}
$$

The first line describes the QD level ϵ closest to the Fermi level (the "resonant" level), subject to an external magnetic field $\vec{E}_Z$ with the components E_x, E_y and E_z expressed in units of energy (i.e., as Zeeman energy contributions). The operator $d_{\sigma}^{\dagger}$ is the creation operator for an electron in the resonant level, and S_x, S_y, S_z are impurity spin operators. The second line describes two superconductors with the dispersion relation ϵ_k and order parameters $\Delta_i \exp(i\phi_i)$. The operator $c_{i,k\sigma}^{\dagger}$ is the creation operator for an electron in the left ($i = $ L) or right ($i = $ R) superconductor, in level k and with spin σ. The third line describes the QD-superconductor hybridisation; we include both spin-preserving and spin-flipping processes with amplitudes $V_{i,k}$ and $W_{i,k}$, respectively. The notation $\bar{\sigma}$ denotes spin inversion, $\bar{\uparrow} = \downarrow$, $\bar{\downarrow} = \uparrow$. Alternatively, we may characterize the tunnel barriers via tunneling rates $\Gamma_L = \pi\rho|V_{L,k_F}|^2$ or $\Gamma_R = \pi\rho|V_{R,k_F}|^2$ for spin-preserving processes, and $\gamma_L = \pi\rho|W_{L,k_F}|^2$ or $\gamma_R = \pi\rho|W_{R,k_F}|^2$ for spin-flip tunneling. Here ρ is the normal-state density of states and we took the matrix elements at the Fermi level, hence at $k = k_F$. Finally, the last line accounts for the presence of all other ("non-resonant") levels in the QD: the electron can also cotunnel through the QD via those high-lying levels, which provides another conduction pathway through the dot. Formally, we may consider this term to arise from integrating out all other levels in the QD, so that

$$
t = \sum_{l,k,k'} \frac{V_{L,k;l}^* V_{R,k';l}}{\Delta \epsilon_l},
\tag{S2}
$$

where we sum over all "non-resonant" levels, $V_{L/R,k;l}$ are the corresponding tunneling amplitude, while $\Delta\epsilon_l$ are the energy levels. (For simplicity, we are disregarding interactions and spin-flip processes.) The inter-lead hopping term makes the model resemble those for a QD embedded in a nanoscopic Aharonov-Bohm ring [3]. The model breaks down if the level spacing is too small (less than the scale of $\Gamma_{L/R}$): in that case one should use a multi-orbital Anderson impurity model instead.

In addition to this last term, we could also include the spin-flip tunneling through high-lying levels, however this brings about no new qualitative effect. As we will show, for what follows, the important element is that the ratio of spin-flip to spin-preserving tunneling rate is different for the resonant level and for the aggregate tunneling rate through all remaining non-resonant levels. This generic situation is expected to hold in most circumstances due to mesoscopic variability of tunneling matrix elements for different QD levels. The hopping elements, $V_{i,k}$, $W_{i,k}$ and t, are in general complex-valued ("directional"): if we reverse the electron flow direction, the amplitude needs to be complex conjugated.

The interacting part of the Hamiltonian is standard:

$$
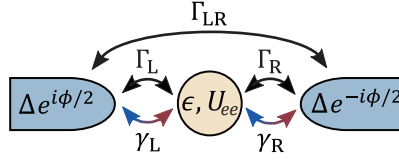H_{\text{int}} = U_{ee} n_{\uparrow} n_{\downarrow},
\tag{S3}
$$

Figure S1. Model diagram of the quantum dot junction. Two s-wave superconductors are connected via tunnelling rates to a single level of a quantum dot. $\Gamma_{L,R}$ and $\gamma_{L,R}$ denote, respectively, the spin-conserving and spin-flipping tunneling rates between the superconducting leads and quantum dot. Γ_{LR} denotes a spin-conserving effective tunneling rate between the superconducting leads via all remaining energy levels, with $\Gamma_{LR} = \pi\rho|t|^2$.

where U_{ee} is the electron-electron repulsion on the QD and $n_\sigma = d_\sigma^\dagger d_\sigma$ is the occupancy operator.

The model is analytically tractable in the regime $\Delta_L, \Delta_R \gg U_{ee}$ (the "superconducting atomic limit" [4–10]) and in the regime $\Gamma_L, \Gamma_R \ll U_{ee}$ (the perturbative limit). We find that it is particularly instructive to integrate out the superconducting electrons and compute the hybridization matrix for this Hamiltonian. This leads to relatively simple closed-form expressions that can be used to construct a highly simplified model. Such a model nevertheless seems to be sufficient to account for the full range of the observed behaviors. The analytic calculations may be verified with explicit calculations using the numerical renormalization group (NRG) techniques, probing their validity over a wide range of parameters.

A. Analytics

We work in the 4×4 Nambu representation with

$$d_a^\dagger = \begin{pmatrix} d_\uparrow^\dagger & d_\downarrow & d_\downarrow^\dagger & d_\uparrow \end{pmatrix}. \tag{S4}$$

Similar notation is used for the c_k operators in the superconducting leads. We will use indexes from the beginning of the alphabet, $a, b, \ldots$, to denote the Nambu-space index $1, 2, 3, 4$. We define the Green's function (GF) matrices $G_{ab}(z) = \langle\langle d_a; d_b^\dagger \rangle\rangle_z$ and $F_{ab,ik}(z) = \langle\langle d_a; c_{ik,b}^\dagger \rangle\rangle_z$; here $\langle\langle A; B \rangle\rangle_z$ denotes the Laplace transform of the Green's function, $\langle\langle A; B \rangle\rangle_z = \int_0^\infty e^{izt} \langle\langle A; B \rangle\rangle_t dt$, where $\langle\langle A; B \rangle\rangle_t = -i\Theta(t)\langle\{A(t), B(0)\}\rangle$ is the retarded GF. In this notation, the equations of motion (EOMs) take the form $z\langle\langle A; B \rangle\rangle_z = \langle\{A, B\}\rangle + \langle\langle A; [H, B] \rangle\rangle_z$. The EOM for the QD take the form

$$z\mathbf{G}(z) = \mathcal{I} + \mathbf{G}(z)\mathbf{H}_0 + \sum_{i,k} \mathbf{F}_{ik}(z)\mathbf{V}_{ik} + \mathbf{U}(z). \tag{S5}$$

Here the argument $z = \omega + i\delta$ is complex frequency, $\mathcal{I}$ is the identity matrix, $\mathbf{H}_0$ corresponds to the Nambu matrix representation of the non-interacting part of the impurity Hamiltonian:

$$\mathbf{H}_0 = \begin{pmatrix} \epsilon + E_z/2 & 0 & (E_x - iE_y)/2 & 0 \\ 0 & -\epsilon + E_z/2 & 0 & -(E_x - iE_y)/2 \\ (E_x + iE_y)/2 & 0 & \epsilon - E_z/2 & 0 \\ 0 & -(E_x + iE_y)/2 & 0 & -\epsilon - E_z/2 \end{pmatrix}, \tag{S6}$$

$\mathbf{V}_{ik}$ contains the hopping matrix elements:

$$\mathbf{V}_{ik} = \begin{pmatrix} V_{i,k} & 0 & iW_{i,k} & 0 \\ 0 & -V_{i,k}^* & 0 & iW_{i,k}^* \\ iW_{i,k} & 0 & V_{i,k} & 0 \\ 0 & iW_{i,k}^* & 0 & -V_{i,k}^* \end{pmatrix}, \tag{S7}$$

and $\mathbf{U}(z)$ contains the contributions of the interacting part of the Hamiltonian, H_{int}. The EOMs for mixed GFs F_{ik} (dropping the frequency argument z in GFs for clarity) may be written as

$$\begin{aligned} \mathbf{F}_{Lk}\left[z\mathcal{I} - \mathbf{H}_{Lk}\right] &= \mathbf{G}\mathbf{V}_{Lk}^\dagger + \mathcal{F}_R\mathbf{T}^*, \\ \mathbf{F}_{Rk}\left[z\mathcal{I} - \mathbf{H}_{Rk}\right] &= \mathbf{G}\mathbf{V}_{Lk}^\dagger + \mathcal{F}_L\mathbf{T}, \end{aligned} \tag{S8}$$

with

$$\mathbf{H}_{ik} = \begin{pmatrix} \epsilon_k & e^{+i\phi_i}\Delta_i & 0 & 0 \\ e^{-i\phi_i}\Delta_i & -\epsilon_k & 0 & 0 \\ 0 & 0 & \epsilon_k & -e^{i\phi_1}\Delta_1 \\ 0 & 0 & -e^{-i\phi_1}\Delta_1 & -\epsilon_k \end{pmatrix}, \tag{S9}$$

$$\mathbf{T} = \begin{pmatrix} t & 0 & 0 & 0 \\ 0 & -t^* & 0 & 0 \\ 0 & 0 & t & 0 \\ 0 & 0 & 0 & -t^* \end{pmatrix}, \tag{S10}$$

and

$$\mathcal{F}_i = \sum_k \mathbf{F}_{ik}. \tag{S11}$$

Using the lead propagator $\mathbf{G}_{ik} = [z\mathcal{I} - \mathbf{H}_{ik}]^{-1}$, this may be rewritten as

$$\mathbf{F}_{\mathrm{L}k} = \mathbf{G}\mathbf{V}_{\mathrm{L}k}^{\dagger}\mathbf{G}_{\mathrm{L}k} + \mathcal{F}_{\mathrm{R}}\mathbf{T}^*\mathbf{G}_{\mathrm{L}k},$$
$$\mathbf{F}_{\mathrm{R}k} = \mathbf{G}\mathbf{V}_{\mathrm{R}k}^{\dagger}\mathbf{G}_{\mathrm{R}k} + \mathcal{F}_{\mathrm{L}}\mathbf{T}\mathbf{G}_{\mathrm{R}k}. \tag{S12}$$

We now assume that V_{ik} and W_{ik} do not depend on k, i.e., $V_{ik} \equiv V_i$ and $W_{ik} \equiv W_i$; this is a reasonable approximation for the relevant bath levels in the vicinity of the Fermi level. We define $\mathbf{G}_i = \sum_k \mathbf{G}_{ik}$ and we sum the EOMs over k:

$$\mathcal{F}_{\mathrm{L}} = \mathbf{G}\mathbf{V}_{\mathrm{L}}^{\dagger}\mathbf{G}_{\mathrm{L}} + \mathcal{F}_{\mathrm{R}}\mathbf{T}^*\mathbf{G}_{\mathrm{L}},$$
$$\mathcal{F}_{\mathrm{R}} = \mathbf{G}\mathbf{V}_{\mathrm{R}}^{\dagger}\mathbf{G}_{\mathrm{R}} + \mathcal{F}_{\mathrm{L}}\mathbf{T}\mathbf{G}_{\mathrm{R}}. \tag{S13}$$

or

$$\begin{pmatrix} \mathcal{F}_{\mathrm{L}} & \mathcal{F}_{\mathrm{R}} \end{pmatrix} \begin{pmatrix} \mathcal{I} & -\mathbf{T}\mathbf{G}_{\mathrm{R}} \\ -\mathbf{T}^*\mathbf{G}_{\mathrm{L}} & \mathcal{I} \end{pmatrix} = \mathbf{G}\begin{pmatrix} \mathbf{V}_{\mathrm{L}}^{\dagger}\mathbf{G}_{\mathrm{L}} & \mathbf{V}_{\mathrm{R}}^{\dagger}\mathbf{G}_{\mathrm{R}} \end{pmatrix}. \tag{S14}$$

The important observation here is that $\mathcal{F}_i$ are proportional to $\mathbf{G}$. This means that the third term in the EOM (S5) can be written as

$$\sum_{ik} \mathbf{F}_{ik}(z)\mathbf{V}_{ik} = \mathbf{G}(z)\mathbf{\Delta}(z), \tag{S15}$$

where $\mathbf{\Delta}(z)$ is the hybridization matrix which describes the renormalization of the QD level due to electron excursions in the superconducting leads. Eq. (S14) can be solved for each $\mathcal{F}_i$ individually, but the expressions are very lengthy and not very informative. Instead, we proceed with calculating the hybridization matrix $\mathbf{\Delta}(z) = [\mathbf{G}(z)]^{-1}\sum_i \mathcal{F}_i \mathbf{V}_i$. We furthermore assume that t is real and introduce the dimensionless quantity $\tilde{t} = \pi\rho t$. We also set $\phi_{\mathrm{L}} = \phi/2$ and $\phi_{\mathrm{R}} = -\phi/2$. Finally, we take the large-Δ limit of the lead propagator

$$\mathbf{G}_{ik} = \frac{1}{z^2 - (\Delta_i^2 + \epsilon_k^2)} \begin{pmatrix} z + \epsilon_k & e^{i\phi_1}\Delta_i & 0 & 0 \\ e^{-i\phi_i}\Delta_i & z - \epsilon_k & 0 & 0 \\ 0 & 0 & z + \epsilon_k & -e^{i\phi_i}\Delta_i \\ 0 & 0 & -e^{-i\phi_i}\Delta_i & z - \epsilon_k \end{pmatrix} \tag{S16}$$

to obtain

$$\mathbf{G}_i = \sum_k \mathbf{G}_{ik} = -\pi\rho \begin{pmatrix} 0 & e^{i\phi_i} & 0 & 0 \\ e^{-i\phi_i} & 0 & 0 & 0 \\ 0 & 0 & 0 & -e^{i\phi_i} \\ 0 & 0 & -e^{-i\phi_i} & 0 \end{pmatrix}. \tag{S17}$$

With these assumptions and simplifications in place, the hybridisation matrix can be written as

$$\mathbf{\Delta}(z) = \frac{\pi\rho}{1 + 2\tilde{t}^2\cos\phi + \tilde{t}^4} \begin{pmatrix} -2a & b & -2c & 0 \\ b^* & 2a & 0 & 2c \\ -2c & 0 & -2a & -b \\ 0 & 2c & -b^* & 2a \end{pmatrix}, \tag{S18}$$

where we introduced the following notation

$$
\begin{aligned}
a &= (V_{\mathrm{L}} V_{\mathrm{R}} + W_{\mathrm{L}} W_{\mathrm{R}}) \tilde{t}(\tilde{t}^2 + \cos\phi), \\
b_i &= V_i^2 + W_i^2, \\
b &= e^{-i\phi/2}(b_{\mathrm{R}} + \tilde{t}^2 b_{\mathrm{L}}) + e^{+i\phi/2}(b_{\mathrm{L}} + b_{\mathrm{R}} \tilde{t}^2), \\
c &= (V_{\mathrm{R}} W_{\mathrm{L}} - V_{\mathrm{L}} W_{\mathrm{R}}) \tilde{t} \sin\phi.
\end{aligned}
\tag{S19}
$$

The key feature of this expression is that this matrix includes terms in the out-of-diagonal 2×2 blocks. These correspond to the presence of an effective magnetic field in the x direction that induces the spin polarization along this same direction. The particular direction (x) results from the assumed form of the spin-orbit-coupling terms in Eq. (S1) and from assuming real $V_{\mathrm{L,R}}$, $W_{\mathrm{L,R}}$ and t. In terms of second quantization operators, the hybridisation matrix corresponds to the following form:

$$
\Delta_{\mathrm{hyb}} = \frac{\pi\rho}{1 + 2\tilde{t}^2 \cos\phi + \tilde{t}^4} \left(-2a \sum_\sigma d_\sigma^\dagger d_\sigma - 4c S_x + b d_\uparrow^\dagger d_\downarrow^\dagger + b^* d_\downarrow d_\uparrow + \mathrm{const.} \right).
\tag{S20}
$$

Not all terms contribute in both spin sectors. The pairing terms proportional to b are only relevant in the spin-singlet sector, while the effective spin-splitting terms proportional to c are only relevant in the spin-doublet sector. The potential term proportional to a contributes in both subspaces. Since we are interested only in the $S = 1/2$ subspace, in the following we concentrate on this particular 2×2 subspace. We find that the effective Hamiltonian of the doublet sector in the $\uparrow, \downarrow$-basis is given by

$$
H_{\mathrm{eff}} = \begin{pmatrix} \epsilon + E_z/2 & (E_x - iE_y)/2 \\ (E_x + iE_y)/2 & \epsilon - E_z/2 \end{pmatrix} - \frac{2\pi\rho}{1 + 2\tilde{t}^2 \cos\phi + \tilde{t}^4} \begin{pmatrix} a & c \\ c & a \end{pmatrix}.
\tag{S21}
$$

This model is exact in the double limit $U_{ee} \to 0$, $\Delta_{\mathrm{L,R}} \to \infty$. In general, one expects correction factors to parameters that depend on both $\Delta_{\mathrm{L,R}}$ and U_{ee}, which control the energy cost of charge fluctuations from the doublet state. These corrections can be accurately computed using the NRG method. Nevertheless, the general form remains the same, as confirmed by numerical calculations, see Sec. II B. Most importantly, the conditions for the matrix element c to be non-zero, as revealed in this calculation, hold fully generally, and are the following: a) the presence of additional QD levels (i.e., nonzero parameter t in the generalized SIAM), b) the presence of both spin-preserving and spin-flip tunneling (so that the combination $V_{\mathrm{R}} W_{\mathrm{L}} - V_{\mathrm{L}} W_{\mathrm{R}}$ is non-zero, which is expected to be generally true except in cases of accidental cancellation), c) finite phase bias ϕ.

We need to note that in the superconducting atomic limit the doublet state in the standard superconducting-SIAM model does not depend on the phase bias ϕ, as can be checked by taking the limit $W_{\mathrm{L,R}} \to 0$ and $t \to 0$ in Eq. (S21). However, away from the superconducting atomic limit an additional diagonal term $E_D \cos(\phi)$ arises, with $E_D > 0$. This term is generated by fourth-order processing in hopping (second order in hybridisation) and has a minimum at $\phi = \pi$ [11], as typical for Josephson junctions with an odd-parity ground state.

Assuming $V_{\mathrm{L}} = V_{\mathrm{R}} \equiv V$, $W_{\mathrm{L}} = -W_{\mathrm{R}} \equiv W$ (note that this sign for W_i choice merely reflects the sign convention in the Hamiltonian and actually corresponds to the symmetric situation with the same amplitude for the left SC to QD and for the QD to right SC spin-flip tunneling), and defining

$$
\Gamma_V = \pi\rho V^2, \quad \Gamma_W = \pi\rho W^2,
$$

the second term of Eq. (S21) can be written as

$$
\frac{2\tilde{t}}{1 + 2\tilde{t}^2 \cos\phi + \tilde{t}^4} \begin{pmatrix} (\Gamma_V - \Gamma_W)(\tilde{t}^2 + \cos\phi) & 2\sqrt{\Gamma_V \Gamma_W} \sin\phi \\ 2\sqrt{\Gamma_V \Gamma_W} \sin\phi & (\Gamma_V - \Gamma_W)(\tilde{t}^2 + \cos\phi) \end{pmatrix}.
\tag{S22}
$$

Assuming that $\tilde{t} \ll 1$, we can simplify the model further by performing a series expansion to obtain

$$
2\tilde{t} \begin{pmatrix} (\Gamma_V - \Gamma_W) \cos\phi & 2\sqrt{\Gamma_V \Gamma_W} \sin\phi \\ 2\sqrt{\Gamma_V \Gamma_W} \sin\phi & (\Gamma_V - \Gamma_W) \cos\phi \end{pmatrix}.
\tag{S23}
$$

Defining

$$
E_t = 2\tilde{t}(\Gamma_V - \Gamma_W), \quad E_{\mathrm{SO}} = 4\tilde{t}\sqrt{\Gamma_V \Gamma_W},
\tag{S24}
$$

we find the approximate small $\tilde{t}$ Hamiltonian given by (up to a constant):

$$H_{\text{eff}} = \begin{pmatrix} E_z/2 & (E_x - iE_y)/2 \\ (E_x + iE_y)/2 & -E_z/2 \end{pmatrix} - \begin{pmatrix} E_t \cos\phi & E_{\text{SO}} \sin\phi \\ E_{\text{SO}} \sin\phi & E_t \cos\phi \end{pmatrix}. \tag{S25}$$

This expression takes the form of the phenomenological potential for the transmon circuit given by main text Eq. (1). Given that there is a potential cancellation of the E_t term, it is prudent to include in the model an addition term of the form $E_D \cos(\phi)$ from processes that are higher-order in hybridisation. This term will combine with $-E_t \cos(\phi)$ to produce the $+E_0 \cos(\phi)$ potential with $E_0 = E_D - E_t$ in Eq. (1). Note that E_0 can take either a positive or negative sign.

Within the limit considered here, we find that E_{SO} depends on each of the three types of coupling in the model: spin-conserving, spin-flipping, and direct lead-lead tunneling. All three have to be present for the spin-splitting to occur. Furthermore, it may happen that the cosine term drops out if the prefactors of all contributions add up to zero, resulting in a Josephson potential shifted by $\pi/2$ compared to the singlet state. This fine-tuned situation is indeed encountered in the experiment as discussed in Sec. V A.

It is instructive to evaluate the eigenvalues of the isolated quantum dot junction. In the simplified model of Eq. (1) these are given by

$$E_{\uparrow,\downarrow} = E_0 \cos\phi \pm \frac{1}{2}\sqrt{E_y^2 + E_z^2 + (E_x - 2E_{\text{SO}} \sin\phi)^2}. \tag{S26}$$

For $E_y = E_z = 0$, this simplifies to

$$E_{\uparrow,\downarrow} = E_0 \cos\phi \pm (E_x/2 - E_{\text{SO}} \sin\phi) \tag{S27}$$

The Zeeman field parallel to E_{SO} enters as a constant offset, which does not change the curvature of the potential and does not affect the transmon frequency. Furthermore, this results in the spin-flip transition frequency given by

$$E_{\uparrow} - E_{\downarrow} = E_x - 2E_{\text{SO}} \sin\phi \tag{S28}$$

which is linear in the applied Zeeman field. Setting $E_x = E_y = 0$ instead, we find

$$E_{\uparrow,\downarrow} = E_0 \cos\phi \pm \frac{1}{2}\sqrt{E_z^2 + 4E_{\text{SO}}^2 \sin^2\phi} \tag{S29}$$

Here the E_z term does enter the curvature of the potential, thus affecting the transmon frequency. Furthermore, the resulting in the spin-flip qubit transition frequency is given by

$$E_{\uparrow} - E_{\downarrow} = \sqrt{E_z^2 + 4E_{\text{SO}}^2 \sin^2\phi} \tag{S30}$$

The presence of the $\sin^2\phi$ term results in the doubling in periodicity we observe in the perpendicular field dependence of main text Fig. 4(c) compared to the parallel field dependence of Fig. 4(b).

B. NRG calculations

The proposed model has very little symmetry: the spin-orbit coupling fully breaks the rotational SU(2) spin symmetry, and the BCS mean-field approximation breaks the U(1) charge conservation. The only remaining symmetry is Z_2 fermionic number parity (even or odd total number of electrons in the system). Furthermore, the Hamiltonian has complex-valued matrix elements. Nevertheless, the quantum impurity problem can still be solved using the conventional impurity solver, the numerical renormalization group (NRG), albeit at quite significant computational cost. The NRG method consists of discretizing the continua (two superconducting baths), their transformation into Wilson tight-binding chains, and an iterative diagonalization of the resulting chain/ladder Hamiltonian. We performed a very coarse discretization with the discretization parameter $\Lambda = 8$; nonetheless, for the purposes of computing energy splitting, this remains a surprisingly good approximation. We retain up to 3000 states in each NRG step. On 8 cores of an AMD EPYC 7452 processor, such NRG calculations take approximately 15 minutes for each parameter set. The band is assumed to have a constant density of states in the interval $[-D : D]$. In the following, all model parameters will be given in units of half-bandwidth D.

We first verify the findings from Supplementary Sec. II A, specifically the spin splitting induced by the combination of the spin-flip scattering, the presence of multiple levels in the QD (represented by the interdot tunneling term t),
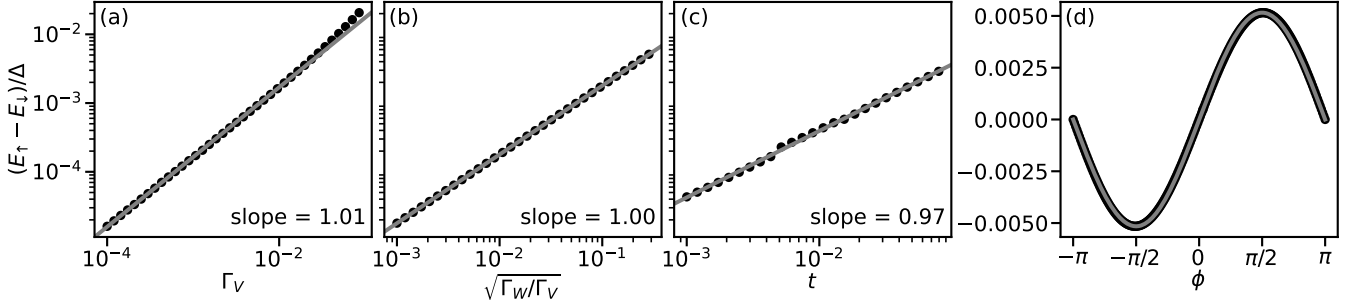
Figure S2. Scaling of the induced spin splitting in the doublet state with parameters Γ_V, Γ_W, and t, as well as the ϕ-dependence. Unless stated otherwise, the parameter set is $U_{ee} = 1$, $\epsilon = -U_{ee}/2$, $\Gamma_V = 0.02$, $\Gamma_W = \Gamma_V/5$, $t = 0.1$, $\Delta = 0.01$, $\phi = \pi/4$. (a) Γ_V-dependence, demonstrating the linearity of splitting as a function of the hybridisation strength, with small non-linear corrections for large Γ_V. (b) Γ_W/Γ_V-dependence, demonstrating the linearity of splitting as a function of the ratio of spin-flip over spin-preserving tunneling processes to the impurity orbital in resonance. (c) t-dependence, demonstrating the linearity of splitting as a function of cotunneling through non-resonant impurity levels. (d) ϕ-dependence, showing a very clean $\sin(\phi)$ behavior of the spin-splitting, as predicted by the reduced analytical model.

and finite superconducting phase difference between the two SC contacts, as described by the $E_{SO} \sin \phi$ terms in the effective Hamilotinian with $E_{SO} = 4\tilde{t}\sqrt{\Gamma_V \Gamma_W} = 4\tilde{t}\Gamma_V \sqrt{\Gamma_W/\Gamma_V}$, see Eqs. (S24) and (S24). In Fig. S2 we plot the dependence of the splitting $E_\uparrow - E_\downarrow$ as a function of key parameters. We indeed observe that the splitting is linear in the hybridisation Γ for fixed Γ_W/Γ_V ratio, in the ratio $W/V = \sqrt{\Gamma_W/\Gamma_V}$ and in the hopping t. Finally, we also ascertain the $\sin(\phi)$ dependence of the splitting. We have thus confirmed that the splitting is linear in t, Γ, W/V, and ϕ for small parameter values.

The dependence on other model parameters, in particular U_{ee} and Δ, is not simple. The parameters U_{ee} and Δ control the energy cost of charge fluctuations, and the behavior depends not only on their ratio, but also on their values compared to the hybridisation Γ as well as the bandwidth D. The simplest case is the linear regime of small parameter Γ, where the splitting is simply inversely proportional to $1/(U_{ee}/2 + \Delta)$ to a good approximation, see Fig. S3(a). For larger Γ, we observe deviations from this simple form, see Fig. S3(b). It is also instructive to consider the dependence on Δ at fixed U_{ee}. The limit of small U_{ee} is merely of academic interest, because the doublet state is then a (highly) excited state: we find a roughly linear dependence on Δ, see Fig. S3(c). For large U_{ee}, however, we find a complex dependence that furthermore depends on the value of Γ, showing a cross-over from quadratic dependence for $\Delta \ll \Gamma$ to a roughly linear dependence for $\Delta \gtrsim \Gamma$, see Fig. S3(d). From these plots we conclude that the dependence on U_{ee}, Δ and Γ (when Γ is not small) is highly non-trivial and should in general be computed numerically (e.g. using the NRG method).

In Fig. S4 we explore the three contributions to the doublet potential: the conventional doublet $E_D \cos(\phi)$ potential with the minima at $\phi = \pm\pi$, the $E_{SO} \sin(\phi)$ potential due to spin-flip scattering with minima at $\phi = \pm\pi/2$, as well as the $-E_t \cos(\phi)$ potential due to cotunneling though the multiple levels of the QD with minimum at $\phi = 0$, see Fig. S4. We plot the results for a range of t starting from zero; this case serves as a reference from which we extract the standard E_D part. With increasing t, both E_{SO} as well as E_t increase. This displaces the minima in the effective potential from $\phi = \pm\pi$ towards $\phi = \pm\pi/2$. When E_t becomes equal to E_D, the $\cos(\phi)$ part of the potential cancels out. For $E_t > E_D$, the minima move past $\phi = \pm\pi/2$ and tend toward $\phi = 0$.

A major time-saving procedure is to incorporate the effects of the external magnetic field as a perturbation to the results of an NRG calculation for a Hamiltonian without any field terms. This ploy rests on the observation that the impurity spin operators are exactly marginal (in the renormalization-group sense): their matrix elements remain of the same order of magnitude throughout the NRG iteration, i.e., they neither blow up nor decay to zero. The method may hence be dubbed the "marginal-operator trick". The idea is to perform the NRG iteration of spin operators S_x, S_y, S_z through unitary transformations to find the effective spin operators in the NRG eigenbasis in the low-energy sector. These are then added to the effective Hamiltonian with bare Zeeman energies E_x, E_y, E_z:

$$H_{\text{eff}} = \sum_w E(w) |w\rangle \langle w| + E_x \tilde{S}_x + E_y \tilde{S}_y + E_z \tilde{S}_z. \tag{S31}$$

Here w indexes the eigenstates $|w\rangle$ with eigenenergies $E(w)$, while $\tilde{S}_i$ are the transformed spin matrices in this same basis. The basis can be truncated to a small number of levels; in many cases it is sufficient to retain solely the subgap states. This effective Hamiltonian may then be diagonalized at negligible numerical cost for arbitrary values of E_x, E_y and E_z. In case where only two (subgap) states are retained one can even write down closed-form expressions for
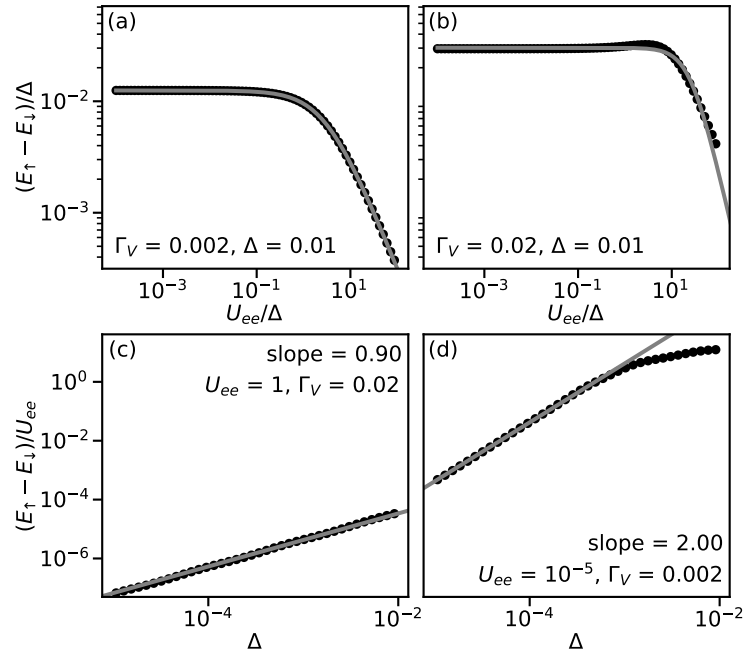
Figure S3. Scaling of the induced spin splitting in the doublet state with parameters U_{ee} and Δ. Other parameters as in Fig. S2. (a) U_{ee}-dependence at $\Gamma_V = 0.002$ showing the cross-over from the $U_{ee} \ll \Delta$ regime to the $U_{ee} \gg \Delta$ regime. (b) Same as a, but for stronger hybridisation $\Gamma_V = 0.02$, showing the more complex behavior away from the low-Γ_V limit. (c) Δ-dependence at $\Gamma_V = 0.02$, showing that the splitting is roughly proportional to Δ in the $U_{ee} \gg \Gamma, \Delta$ regime. (d) Same as (c), but for $\Gamma_V = 0.002$ and much smaller $U_{ee} = 10^{-5}$ (non-interacting limit), showing quadratic scaling for $\Delta \ll \Gamma$ that crosses over into linear scaling for $\Delta \gg \Gamma$.
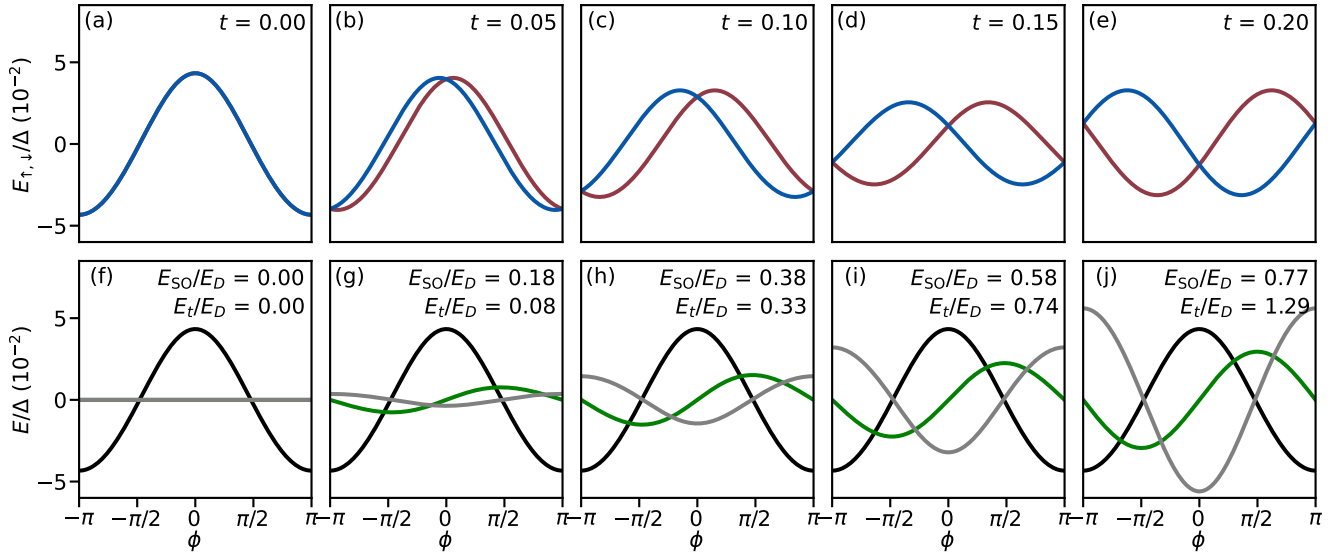

Figure S4. Decomposition of the doublet potential energy into its components. We show the results for various values of t, as indicated for each panel. All plots have the same axis ranges in order to permit direct comparison of magnitudes. (a-e) Total potential for the two spin states. (f-g) $E_D \cos(\phi)$ potential, common to all cases (black), $-E_t \cos(\phi)$ (green) and $E_{SO} \sin(\phi)$ (grey) contributions. We find $E_D = 4.33 \, 10^{-3}$ (same for all t) and the E_t/E_D and E_{SO}/E_D ratios indicated for each panel. Other model parameters are $U_{ee} = 1$, $\epsilon = -U_{ee}/2$, $\Delta = 0.1$, $\Gamma_V = 0.2$, $\Gamma_W/\Gamma_V = 1/5$.

eigenenergies and eigenstates. The marginal-operator trick is a good approximation up to Zeeman energies comparable to the BCS energy gap Δ, as it has been ascertained by comparisons with the NRG calculations with the Zeeman terms included from the outset, see Fig. S5. This method is clearly very generally applicable to any problem involving
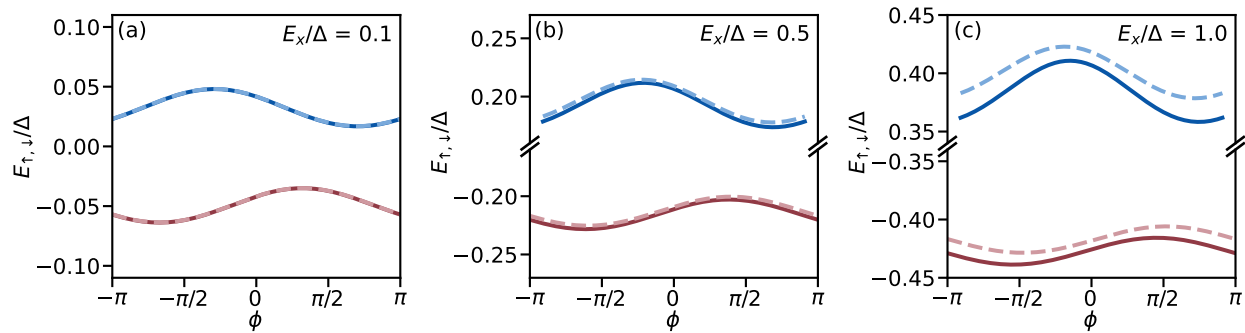
Figure S5. Comparison of the energies of the doublet subgap states as a function of the phase bias computed using the standard NRG procedure (solid lines) and using the "marginal-operator trick" approximation (discontinuous lines). Vertical scale is the same for all panels. Model parameters are $U_{ee} = 1.5$, $\Gamma_{\rm L} = \Gamma_{\rm R} \equiv \Gamma = 0.2$, $\gamma_{\rm L} = \gamma_{\rm R} = 0.2\Gamma$, $t = 0.1$, $\epsilon = 0.1 - U_{ee}/2$, $\Delta = 0.1$.

marginal operators in the Hamiltonian, obviating the need for costly parameter sweeps in multidimensional spaces.

C. Transmon diagonalization

Having established how to calculate an effective potential in the doublet sector, we now turn to its inclusion in the Hamiltonian of the encompassing transmon circuit [12]:

$$H = -4E_{\rm c}\partial_\phi^2 + E_{\rm J}(1 - \cos\delta) + U(\phi), \tag{S32}$$

where $E_{\rm c}$ and $E_{\rm J}$ denote the charging energy of the transmon island and the Josephson energy of the reference junction, respectively, and $U(\phi)$ denotes the effective doublet potential of main text Eq. (1). The two phase drops across the quantum dot junction (ϕ) and across the reference junction (δ) are connected according to $\phi - \delta = \phi_{\rm ext}$, where $\phi_{\rm ext} = (2e/\hbar)\Phi_{\rm ext}$ is the phase difference resulting from the externally applied magnetic flux through the SQUID loop, $\Phi_{\rm ext}$ [Fig. 1(d)].

Following [13, 14], we numerically diagonalize (S32) in the phase basis. This results in the energy levels E_n as well as the associated transition frequencies $f_{nm} = (E_m - E_n)/h$, capturing both the transmon and the spin-flip transitions. Having calculated the transition frequencies, fits can be made to the data. This is done to obtain the estimates for the effective model parameters found in the main text and in the next sections, using $E_{\rm c}/h = 284\,\rm MHz$ and $E_{\rm J}/h = 12.4\,\rm GHz$ to $12.7\,\rm GHz$ as reference junction parameters. Note that the reference junction gate voltage is generally held fixed in the experiment, and that the range in $E_{\rm J}$ is the result of cross-coupling between the quantum dot and reference junction gate lines.

Here we note that the sinusoidal reference junction potential used in Eq. (S32) is that of a conventional superconductor-insulator-superconductor (SIS) tunnel junction, governed by many weakly transparent channels. Previous work has found that nanowire-based Josephson junctions are more accurately described by several or even a single transport channel, leading to a more skewed potential shape [15]. This can result in a reduction of the the qubit anharmonicity, and thus an underestimation of $E_{\rm c}$ when using the SIS potential. However, the inclusion of a more involved potential introduces additional fitting parameters, and obtaining unique solutions is not guaranteed. This holds in particular because the reference junction is operated far from its pinchoff voltage, such that several channels are expected to contribute to the potential (see Sec. IV). We therefore choose to use the SIS potential throughout the Letter. In practice, this choice affects the value of $E_{\rm c}$ that is extracted from the fit, which in turn rescales the extracted values of E_0 and $E_{\rm SO}$.

III.   DEVICE AND EXPERIMENTAL SETUP

A.   Device overview

The physical implementation of the device studied is shown in Fig. S6. It is analogous to that of [2], repeated here for convenience. The chip, 7 mm long and 2 mm wide, consists of four devices coupled to a single transmission line with an input capacitor to increase the directionality of the outgoing signal [Fig. S6(b)]. For the experiments performed in this Letter only two of the devices were wire-bonded: the device measured in the main text, and a second device, which was not functional.

For each device, a lumped element readout resonator is capacitively coupled to the feedline [Fig. S6(c)]. The resonator is additionally capacitively coupled to the transmon island, which is connected to ground via a SQUID loop formed by the reference and quantum dot junctions [Fig. S6(d)]. Both junctions are implemented on a single 10 um-long epitaxial superconductor-semiconductor nanowire with a 110 nm-wide hexagonal InAs core and a 6 nm-thick Al shell covering two of its facets, in turn covered by a thin layer of aluminium oxide. The growth conditions were almost identical to those detailed in Ref. [16], with the only two differences being that this time the As/In ratio is 12, smaller than in Ref. [16], and that the oxidation of the Al shell is now performed in-situ, for better control, reproducibility and homogeneity of the oxide layer covering the shell. Inspection of the nanowire batch, performed under a scanning electron microscope directly after growth, indicated an average wire length of $9.93\pm 0.92\,\mu m$ and an average wire diameter of 111 ± 5 nm. For the device investigated here, the two facets of the aluminum shell are situated on the top part of the nanowire. The two junctions are defined in two uncovered nanowire sections (110 nm-long for the reference junction and 200 nm-long for the quantum dot junction). A zoom-in of the the quantum dot junction is shown in Fig. S6(e). The reference junction is controlled by a single 110 nm-wide electrostatic gate, set at a DC voltage V_J. The quantum dot junction is defined by three 40 nm-wide gates separated from each other by 40 nm. We note that in Fig. 1(e) the gates appear wider (and the gaps between gates appear smaller) than stated due to distortion by the gate dielectric layer. The outer two gates are set at DC voltages V_L and V_R. The central gate is connected to a bias-tee formed by a $100\,k\Omega$ resistor and a 100 pF capacitor. This permits the simultaneous application of a DC signal V_C to control the level of the quantum dot junction and a microwave tone $f_{s,drive}$ to drive the spin-flip transition.

B.   Nanofabrication details

The device fabrication occurs in several steps using standard nanofabrication techniques. It is identical to that described in [2], and repeated here for the sake of completeness. The substrate consists of 525 µm-thick high-resistivity silicon, covered in 100 nm of low pressure chemical vapor deposited Si_3N_4. On top of this, a 20 nm thick NbTiN film is sputtered, into which the gate electrodes and circuit elements are patterned using an electron-beam lithography mask and SF_6/O_2 reactive ion etching. Subsequently, 30 nm of Si_3N_4 dielectric is deposited on top of the gate electrodes using plasma enhanced chemical vapor deposition and then etched with a buffered oxide etchant. The nanowire is then deterministically placed on top of the dielectric using a nanomanipulator and an optical microscope. After placement, two sections of the aluminium shell are selectively removed by wet etching with MF-321 developer. These sections form the quantum dot junction and the reference junction, with lengths 200 nm and 110 nm respectively. After the junction etch, the nanowire is contacted to the transmon island and to ground by an argon milling step followed by the deposition of 150 nm-thick sputtered NbTiN. Finally, the chip is diced into 2 by 7 millimeters, glued onto a solid copper block with silver epoxy, and connected to a custom-made printed circuit board using aluminium wirebonds.
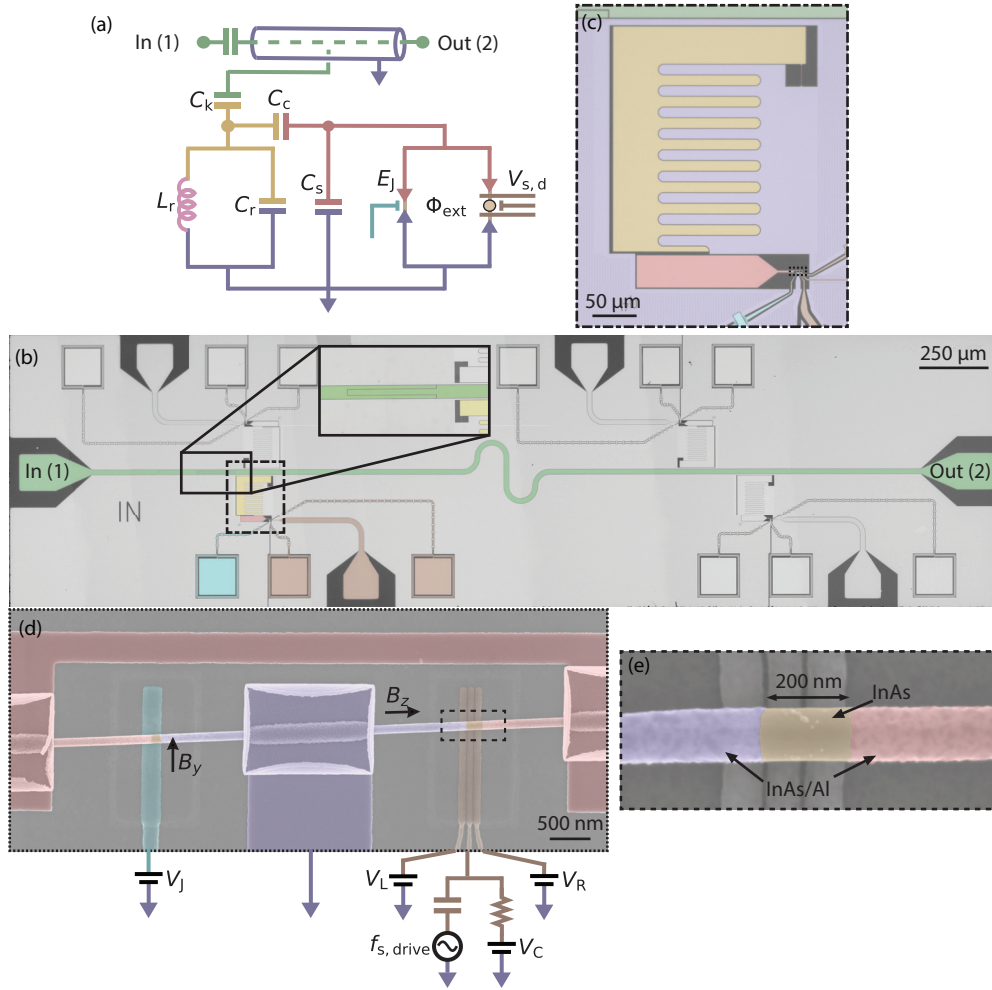
Figure S6. **Device overview.** (a) Diagram of the microwave circuit. A coplanar waveguide transmission line with an input capacitor (green center conductor) is capacitively coupled to a grounded LC resonator. The resonator consists of an island (yellow) capacitively and inductively (pink) shunted to ground (blue). The resonator is in turn capacitively coupled to a transmon island (red), which is shunted to ground capacitively as well as via two parallel Josephson junctions. (b) Chip containing four nearly identical devices coupled to the same transmission line, which has an input capacitor, enlarged in inset. (c) False-colored optical microscope image of the device showing the qubit island, the resonator island, the resonator inductor, the transmission line, the electrostatic gates and ground. (d) False-colored scanning electron micrograph (SEM) of the measured device, showing the InAs/Al nanowire into which the junctions are defined. The B_y component of the magnetic field is used to tune Φ_{ext} [17]. B_z is the magnetic field component parallel to the nanowire. (e) False-colored SEM of the measured device, showing the quantum dot junction in which the quantum dot is gate defined. The three bottom gates have a width and spacing of 40 nm, although this is obfuscated by the dielectric layer placed on top.

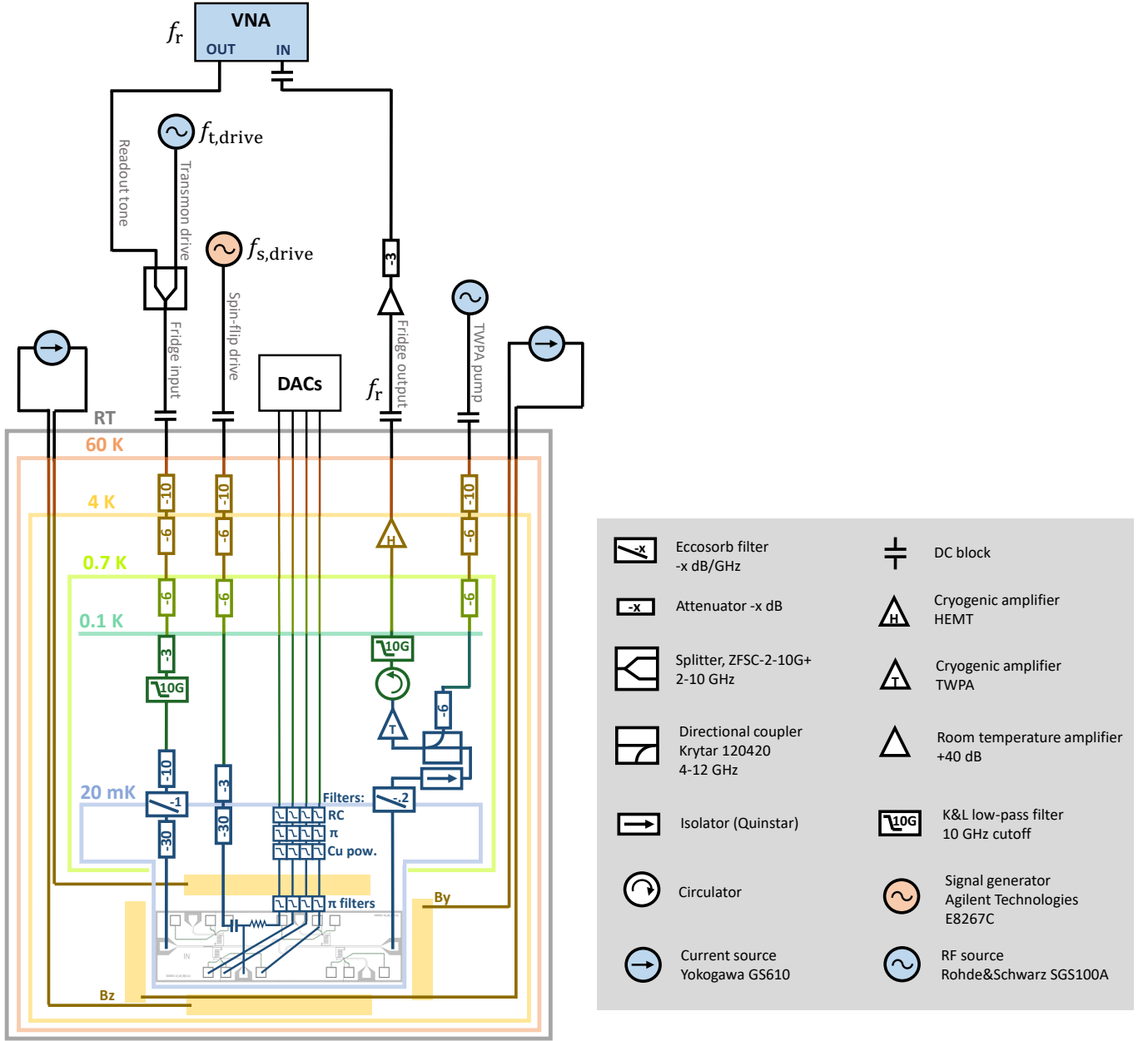## C. Cryogenic and room temperature measurement setup

Figure S7. **Measurement setup at cryogenic and room temperatures.** The device was measured in a Triton dilution refrigerator with a base temperature of 20 mK. The setup contains an input RF line, an output RF line, an additional RF line for driving the spin-flip transition, and multiple DC gate lines. The DC gate lines are filtered at base temperature with multiple low-pass filters connected in series. The input and drive RF lines contain attenuators and low-pass filters at different temperature stages, as indicated. The output RF line contains a travelling wave parametric amplifier (TWPA) at the 20 mK temperature stage, a high-electron-mobility transistor (HEMT) amplifier at the 4 K stage, and an additional amplifier at room temperature. A three-axis vector magnet (x-axis not shown) is thermally anchored to the 4 K temperature stage, with the device under study mounted at its center. The three magnet coils are controlled with Yokogawa GS610 current sources. At room temperature, a vector network analyzer (VNA) is connected to the input and output RF lines for spectroscopy at frequency f_r. On the input line, this signal is then combined with the transmon drive tone at frequency $f_\text{t,drive}$, for two-tone spectroscopy. The spin-flip drive tone at frequency $f_\text{s,drive}$ is sent through the additional RF line.

IV. BASIC CHARACTERIZATION AND TUNE UP

This section describes how the device is tuned to its gate setpoints.
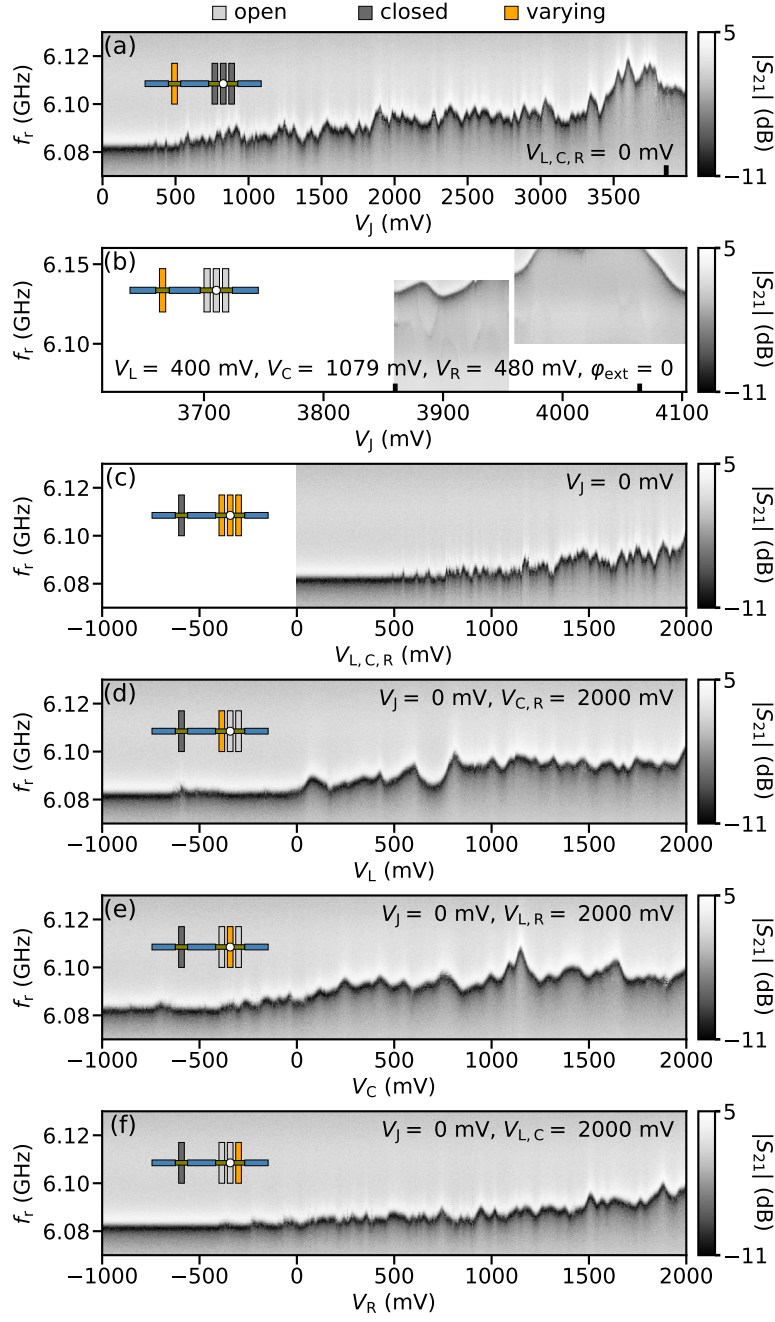

Figure S8. **Electrostatic gates characterization.** Transmission amplitude as a function of frequency of a single tone f_r and gate voltage. For each panel, the inset indicates which gate is being varied (orange) and which ones are set to a value above (light grey) or below (dark grey) their pinch-off value.

We start by characterizing the effect of the electrostatic gates, which control each of the two Josephson junctions. Fig. S8(a) shows the basic behaviour of the reference junction versus junction gate voltage V_J when the quantum dot junction is completely closed. As V_J is varied, different junction channels open sequentially [18, 19], with transparencies that increase non-monotonically due to mesoscopic fluctuations. This in turn affects the E_J of the transmon, allowing for in-situ tunability of its frequency, and the transmon then affects the resonator through its dispersive shift [20],

resulting in the observed change in resonator frequency. We use this to choose a V_J set-point which maintains a good SQUID asymmetry in all regimes of interest. The black line in Fig. S8(a) indicates $V_J = 3860\,$mV, the setpoint used in Figs. 3(a-b) in the main text, which fixes the transmon frequency at $f_t = 4.7\,$GHz. After changing the quantum dot junction from gate setpoint A to gate setpoint B and due to cross-coupling between the quantum dot and reference gates, the reference junction started exhibiting poisoning behavior. Therefore, its setpoint was then set to $V_J = 4064.5\,$mV, fixing the transmon frequency at $f_t = 4.95\,$GHz, which was used for all other data shown in the main text. Fig. S8(b) shows a measurement taken at the moment when the V_J value was changed from its $V_J = 3860\,$mV to its $V_J = 4064.5\,$mV setpoint, both indicated with black lines. For all resonances explored, we maintained $E_J/E_c > 40$.

In Figs. S8(c-f) we show analogous measurements where we vary the quantum dot gate voltages when the reference junction is closed. We first measure an effective pinch-off curve for all three quantum dot gates ramped together [Fig. S8(c)], before sweeping each gate separately, with the other two quantum dot gates kept at 2000 mV [Figs. S8(d-f)]. This shows that each of the three quantum dot gates can independently pinch off the quantum dot junction, even if the other gates are in the open regime, signifying strong lever arms and good gate alignment. Note that these are not pinch-off curves as encountered in conventional tunnel spectroscopy; they reflect the voltages at which there is no longer a measurable transmon transition frequency mediated by the quantum dot junction, which could either be due to low tunneling rates or a full depletion of the quantum dot.

The subsequent tuning procedure for finding an isolated quantum dot resonance is discussed in detail in Ref. [2], summarized here for the specific resonances used in the main text. First we close the reference junction and go to a point in quantum dot gate voltages near pinchoff. Fixing the readout frequency f_r at the bare frequency of the resonator, one can then map out the regions where dispersive shifts occur on a two-dimensional map versus the left and right quantum dot gates, with the central gate held fixed. This signifies regions in which there is a supercurrent flowing through the quantum dot junction. After identifying such a region in V_L-V_R space, we subsequently open the reference junction, which lifts the reference transmon frequency closer to the bare resonator frequency. This magnifies the dispersive shift of the resonator and, furthermore, brings the external flux into the picture. Fixing $\phi_{ext} = 0$ and repeating the initial measurement then reveals much stronger deviations of the resonant frequency due to the enhanced dispersive shift.
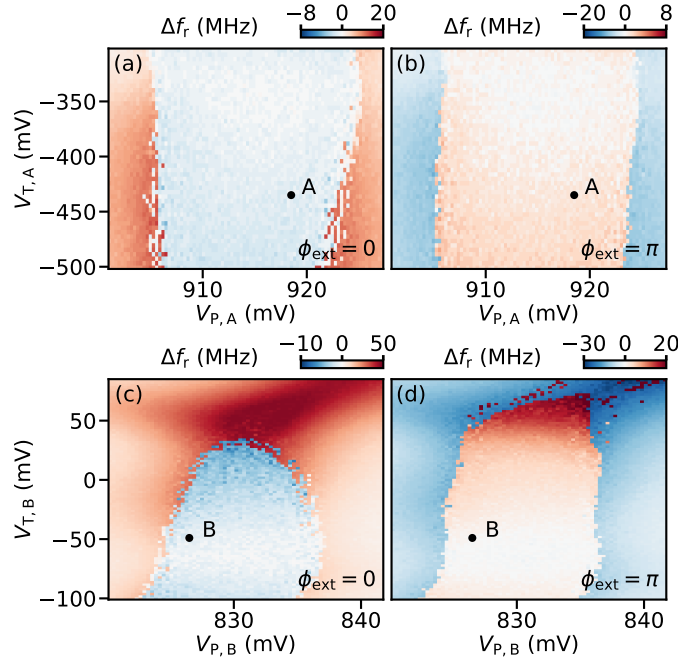

Figure S9. (a,c) Shift of the resonator resonance frequency with respect to its value when the quantum dot junction is fully closed, Δf_r, versus V_P and V_T at $\phi_{ext} = 0$, revealing singlet (red) and doublet (blue) ground state regions separated by sharp transitions for resonance A (a) and resonance B (c). (b,d) Same as (a,c) but for $\phi_{ext} = \pi$. The markers indicate the gate setpoints used in the main text, A and B.

Using this approach we identify isolated quantum dot resonances, and subsequently explore their evolution versus the central quantum dot gate. This is shown in Fig. S9, where we furthermore account for cross coupling between

the different quantum dot gates by defining a new set of virtual gates. For simplicity we fix V_{L} and focus on the rotated V_{R}-V_{C} space, denoted as the V_{P}-V_{T}-space. Note that this compensation scheme is unique for each isolated region we explore. Fixing $\phi_{\mathrm{ext}} = 0$ and varying the central dot gate, the resonator first shows a displacement towards higher frequencies to then abruptly drop to a lower frequency, to then finally go back to the higher frequencies once-more [Fig. S9(a,c)]. This behaviour is reversed for $\phi_{\mathrm{ext}} = \pi$ [Fig. S9(b,d)], and can be identified as a singlet-doublet transition resulting from the relative level of the quantum dot is being varied by V_{P} [2]. We note that in the V_{T} direction we do not always find the expected dome shape characteristic of singlet-doublet transitions; while such a shape does develop for resonance B [Fig. S9(c-d)], the doublet phase of resonance A [Fig. S9(a-b)] remains open even at elevated tunnel gate voltages. This is potentially a result of a non-monotonic dependence of tunnel rates on the gate voltage.

V. EXTENDED DATA

A. Spin-orbit splitting at different resonances

As discussed in the main text, we find a wide variety of phase-dependent splittings depending on the quantum dot resonance studied. This is shown in Fig. S10, portraying a range of resonances all the way from an even phase dependence with no splitting (panel d) to resonances that have a fully odd phase dependence (panel b). By Fitting the potentials with the transmon Hamiltonian, as dicussed in Sec. II C, we extract a set of effective parameters for each resonance, tabulated in Table I.
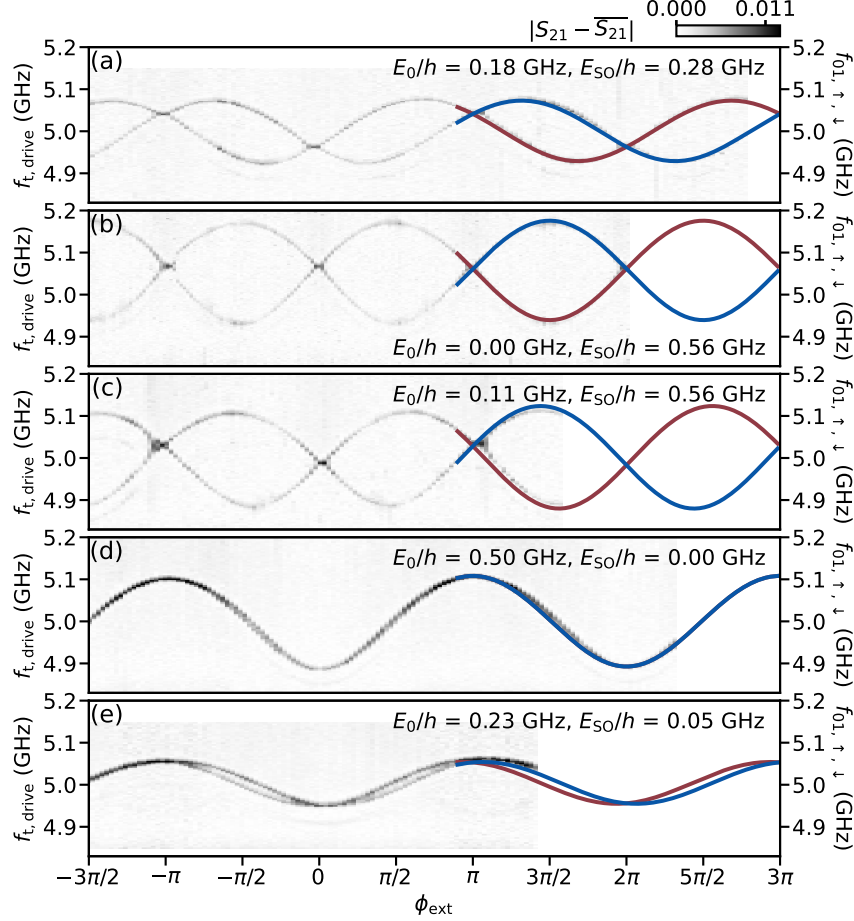

Figure S10. **Spin-splitting energies at different resonances.** Flux dependence of transmon spectroscopy taken at different points in quantum dot gate space, indicated in Table I. In all cases, the quantum dot junction is in a doublet state. Different panels show different spin-splitting energies. (a) and (b) are gate setpoints A and B of the main text, respectively.

Table I. Quantum dot junction gate voltage set points and extracted model parameters for the five panels in Fig. S10.

	V_L (mV)	V_C (mV)	V_R (mV)	E_0/h (GHz)	E_{SO}/h (GHz)
(a)[a]	79.0	1020.0	363.0	0.18	0.28
(b)[b]	430.0	531.0	635.2	0.00	0.56
(c)	430.0	520.0	652.0	0.11	0.56
(d)	430.0	614.8	335.0	0.50	0.00
(e)	430.0	655.2	305.2	0.23	0.05

[a] Gate setpoint A in the main text figures.
[b] Gate setpoint B in the main text figures.

B.   Spin-orbit splitting within the same resonance

Within the extended SIAM model, E_{SO} and E_0 are expected to depend on Γ_V, Γ_W, and $\tilde{t}$ (see Sec. II). One would therefore expect that these quantities can also vary within a single resonance, as the gate voltages tune the relative energy levels as well as the tunnel barriers of the quantum dot. This is indeed observed in the experiment: as shown in Fig. S11(a,b) for resonance A, we find that both effective doublet parameters vary with the rotated plunger and tunnel gates. In particular, both E_0 and E_{SO} show an increase towards the boundary of the singlet doublet transition, i.e. towards the edges of the Coulomb diamond. This is in line with the predictions of Ref. [21], as in the middle of the Coulomb diamond the energy cost of adding an electron to the quantum dot is maximal and the high energy of the intermediate states reduces the probability of Cooper pair tunneling. Additionally, contrary to initial expectation, the magnitude of the effective parameters appears to decrease for larger tunnel gate values. While the tunnel gate is expected to increase the tunnel rates, and thus the effective parameters, we note that in practice the situation is highly complex; there are up to three gate voltages that control five model parameters ($\Gamma_{V,W}^{\mathrm{L,R}}$, $\tilde{t}$), with potentially non-monotonic dependencies as well as cross-coupling. A full understanding of such a system will require a more detailed study of such dependencies, which we leave for future work. At this stage we instead emphasize the gate-tunability of these quantities, allowing for in-situ fine-tuning of the model parameters

Furthermore, we also find that the effective Landé g-factor g^* depends on gate voltage [Fig. S11(c)], in line with previous results on quantum dots in InAs nanowires, demonstrating its electric gate tunability [22]. This could be of relevance for qubit applications, as the tunability can be used to rapidly drive spin states in and out of resonance with a static magnetic field induced electron spin resonance condition. Finally, we note that the observed gate dependence of g^* is distinct from that of E_{SO} and E_0, supporting the assertion that its origin is tied to a complex interplay of spin-orbit coupling and confinement, beyond the model considered here [23–25].
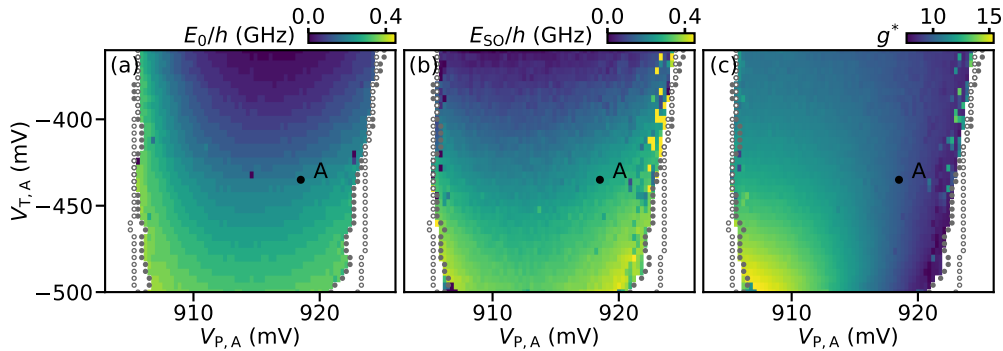

Figure S11.   **Gate dependence within resonance A.** (a) Magnitude of E_0 extracted from transmon qubit spectroscopy at $\phi_{\mathrm{ext}} = 0, \pi$ versus rotated plunger and tunnel gate voltages, at a magnetic field of $18\,\mathrm{mT}$ applied parallel to the nanowire. (b) Same as (a) for E_{SO}, extracted from spin-flip spectroscopy at $\phi_{\mathrm{ext}} = \pi/2, 3\pi/2$. (c) Same as (b) for g^*, extracted from the same measurement as (b).

C.   Magnetic field angle dependence and determination of the spin-splitting direction

In this Section we detail the method used to determine the direction of the spin-orbit interaction at a fixed gate point (vector $\vec{n}$ in Eq. 1 in the main text). This is done by comparing the angle dependence of transmon and spin-flip spectroscopy to the predictions of the model discussed in Sec. II. For this it is useful to define a coordinate space determined by the nanowire direction, Z, the on-chip direction perpendicular to the nanowire, Y, and the direction perpendicular to the chip, X. We then define $\theta \in [0, 180)$ as the polar angle with respect to the Z direction and $\phi \in [0, 360)$ as the azimuthal angle [see Fig. S12], such that $B_x = B_r \cos(\phi)\sin(\theta)$, $B_y = B_r \sin(\phi)\sin(\theta)$ and $B_z = B_r \cos(\theta)$. Note that the cartesian field directions B_x, B_y and B_x set a frame of reference and should not be confused with the directions $B_\parallel$ and $B_\perp$ presented in the main text, which are specific for each gate setpoint. With this convention, $\phi = 90$ is the plane of the chip, while $\phi = 0$ is the plane perpendicular to the chip containing the nanowire. In each of these two planes, we first fix the magnitude of the applied magnetic field, B_r, and measure the evolution of transmon and spin-flip spectroscopy while varying θ in steps of two degrees. For each plane we determine the angle for which the applied field is perpendicular to the spin-splitting direction, $\theta_{\perp,0}$ and $\theta_{\perp,90}$, by comparison to the theory model. The cross product of these two directions determines the direction parallel to the spin-splitting term.

Representative data of such a measurement for resonance A is shown in Fig. S12(a-b), where we fix $\phi = 90$ and find $\theta_{\perp,90} = 78$. Performing an analogous measurement in the $\phi = 0$ plane, we determine $\theta_{\perp,0} = 86$. From these two, we obtain $(\theta_s, \phi_s) = (167, 72)$ as the spin-splitting direction $\vec{n}$ of resonance A. This is 13 degrees away from the nanowire axis. Furthermore, we generally find that the measured spin-split direction varies depending on which quantum dot resonance is studied; for resonance B of the main text we obtain a spin-splitting direction of $(\theta_s, \phi_s) = (72, 45)$, which is 84 degrees away from the spin-splitting direction of resonance A.

We can furthermore estimate the effective Landé g-factor from the evolution of the spin-flip transition frequency versus the angle of the magnetic field. Shown in Fig. S12(c) for resonance A, the effective g-factor varies from 3 to 11 depending on the angle, minimal for magnetic fields perpendicular to the spin-orbit direction. The measured behaviour is well-described by a simple cosine, in line with previous results on quantum dots in InAs nanowires [24].
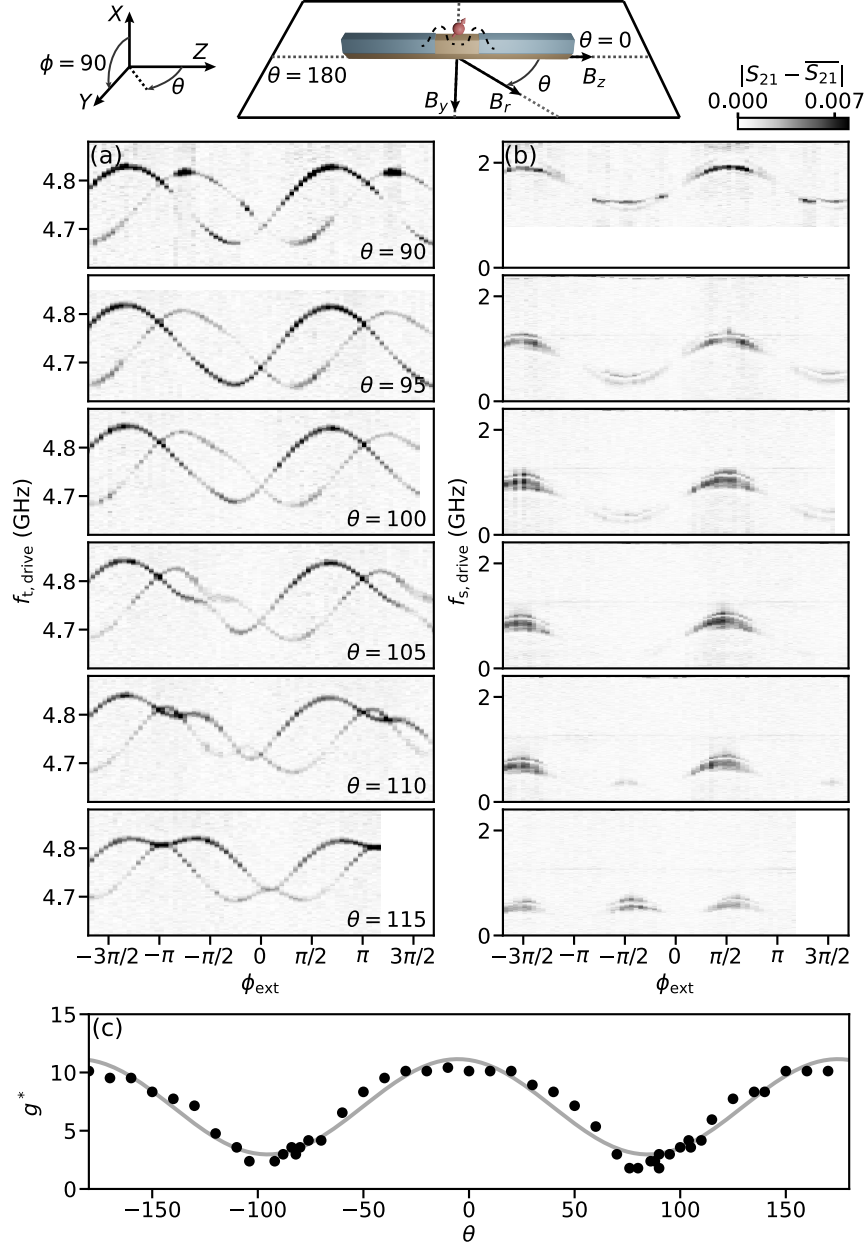

Figure S12. **Magnetic field angle dependence of resonance A.** (a-b) Flux dependence of transmon (left column) and spin-flip (right column) transitions for different magnetic field directions, for a fixed total magnetic field $B_r = 12\,\text{mT}$. Each row corresponds to a different magnetic field orientation on the chip plane, $\phi = 90$, determined by the angle θ with respect to the nanowire direction (see diagram at the top). All panels share the same color bar. (c) Effective Landé g-factor g^* versus θ. Markers show data extracted from spin-flip spectroscopy at $12\,\text{mT}$, and the solid line shows a fit with a cosine.

D. Spin-flip spectroscopy enabled by spin-orbit splitting

As discussed in the main text, we do not rely on driving transitions of the transmon circuit to perform spectroscopy of the junction's excitation spectrum. While in principle possible by using three microwave tones, this could result in limitations due to the finite transmon lifetime as well as undesired mixing processes between the different tones. Instead, we use the dispersive shift from the transmon's ground state to induce a doublet-state-dependent shift on the resonator, similar to how the island parity of offset-charge sensitive transmon qubits can be distinguished [26, 27]. As the difference between the transmon frequencies of both doublet states is small, inducing a sizeable dispersive shift larger than the resonator's linewidth requires us to tune the spin-dependent transmon qubit frequency close to that of the resonator [Fig. S6(a-b)]. Having done so, we can observe the spin-flip transition directly with conventional two-tone spectroscopy, where the first tone is applied at the frequency of the readout resonator, and the second tone at the spin-flip frequency [Fig. S6(c)]. The transmon, off-resonant from both tones, remains in its ground state during the measurement.
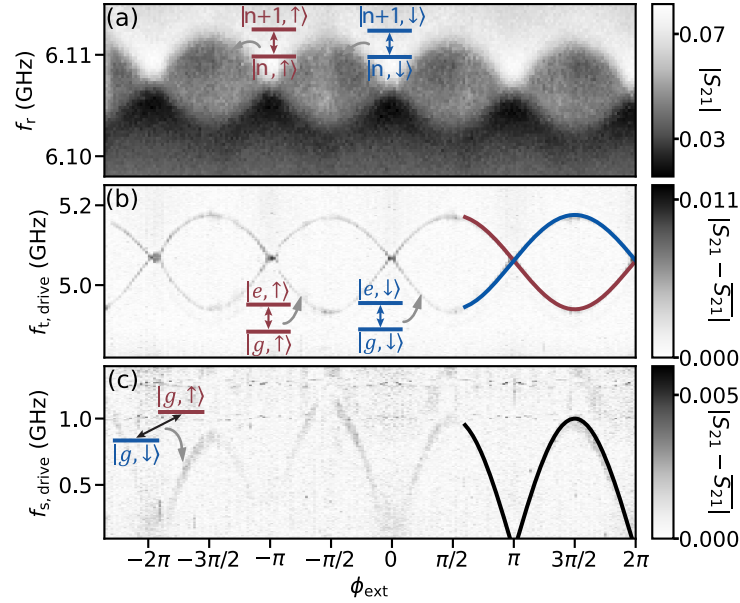

Figure S13. **Spin-flip two-tone spectroscopy.** (a) Flux dependence of single-tone spectroscopy showing the resonator frequency. Each of the two visible branches corresponds to a different spin state of the quantum dot junction. (b) Flux dependence of two-tone spectroscopy showing the transmon frequency. The continuous lines denote the two transmon branches corresponding to the two possible spin states of the quantum dot junction. They are the result from the same fit as in Fig. S10. (c) Flux dependence of two-tone spectroscopy showing the spin-flip frequency. The continuous line denotes the spin-flip transition frequency obtained from the same fit as in Fig. S10.

[1] V. Meden, The Anderson–Josephson quantum dot—a theory perspective, J. Phys. Condens. Matter **31**, 163001 (2019).
[2] A. Bargerbos, M. Pita-Vidal, R. Žitko, J. Ávila, L. J. Splitthoff, L. Grünhaupt, J. J. Wesdorp, C. K. Andersen, Y. Liu, L. P. Kouwenhoven, R. Aguado, A. Kou, and B. van Heck, Singlet-doublet transitions of a quantum dot josephson junction detected in a transmon circuit, PRX Quantum **3**, 030311 (2022).
[3] C. Karrasch and V. Meden, Supercurrent and multiple singlet-doublet phase transitions of a quantum dot Josephson junction inside an Aharonov-Bohm ring, Phys Rev B **79**, 045110 (2009).
[4] I. Affleck, J.-S. Caux, and A. M. Zagoskin, Andreev scattering and Josephson current in a one-dimensional electron liquid, Phys Rev B **62**, 1433 (2000).
[5] A. Rozhkov and D. Arovas, Interacting-impurity Josephson junction: Variational wave functions and slave-boson mean-field theory, Phys. Rev. B **62**, 6687 (2000).
[6] E. Vecino, A. Martín-Rodero, and A. Levy Yeyati, Josephson current through a correlated quantum level: Andreev states and π junction behavior, Phys. Rev. B **68**, 035105 (2003).

[7] A. Oguri, Y. Tanaka, and A. C. Hewson, Quantum phase transition in a minimal model for the Kondo effect in a Josephson junction, J. Phys. Soc. Japan **73**, 2494 (2004).

[8] Y. Tanaka, A. Oguri, and A. C. Hewson, Kondo effect in asymmetric Josephson couplings through a quantum dot, New J Phys **9**, 115 (2007).

[9] C. Karrasch, A. Oguri, and V. Meden, Josephson current through a single Anderson impurity coupled to BCS leads, Phys. Rev. B **77**, 024517 (2008).

[10] T. Meng, S. Florens, and P. Simon, Self-consistent description of Andreev bound states in Josephson quantum dot devices, Phys. Rev. B **79**, 224521 (2009).

[11] B. I. Spivak and S. A. Kivelson, Negative local superfluid densities: The difference between dirty superconductors and dirty Bose liquids, Phys. Rev. B **43**, 3740 (1991).

[12] J. Koch, T. M. Yu, J. Gambetta, A. A. Houck, D. I. Schuster, J. Majer, A. Blais, M. H. Devoret, S. M. Girvin, and R. J. Schoelkopf, Charge-insensitive qubit design derived from the cooper pair box, Phys. Rev. A **76**, 042319 (2007).

[13] A. Bargerbos, W. Uilhoorn, C.-K. Yang, P. Krogstrup, L. P. Kouwenhoven, G. de Lange, B. van Heck, and A. Kou, Observation of vanishing charge dispersion of a nearly open superconducting island, Phys. Rev. Lett. **124**, 246802 (2020).

[14] A. Kringhøj, T. W. Larsen, B. van Heck, D. Sabonis, O. Erlandsson, I. Petkovic, D. I. Pikulin, P. Krogstrup, K. D. Petersson, and C. M. Marcus, Controlled DC monitoring of a superconducting qubit, Phys. Rev. Lett. **124**, 056801 (2020).

[15] A. Kringhøj, L. Casparis, M. Hell, T. W. Larsen, F. Kuemmeth, M. Leijnse, K. Flensberg, P. Krogstrup, J. Nygård, K. D. Petersson, and C. M. Marcus, Anharmonicity of a superconducting qubit with a few-mode Josephson junction, Phys. Rev. B **97**, 060508(R) (2018).

[16] P. Krogstrup, N. L. B. Ziino, W. Chang, S. M. Albrecht, M. H. Madsen, E. Johnson, J. Nygård, C. Marcus, and T. S. Jespersen, Epitaxy of semiconductor-superconductor nanowires, Nat. Mater. **14**, 400 (2015).

[17] J. J. Wesdorp, L. Grünhaupt, A. Vaartjes, M. Pita-Vidal, A. Bargerbos, L. J. Splitthoff, P. Krogstrup, B. van Heck, and G. de Lange, Dynamical polarization of the fermion parity in a nanowire Josephson junction, arXiv e-prints (2021), arXiv:2112.01936.

[18] E. M. Spanton, M. Deng, S. Vaitiekėnas, P. Krogstrup, J. Nygård, C. M. Marcus, and K. A. Moler, Current–phase relations of few-mode InAs nanowire Josephson junctions, Nat. Phys. **13**, 1177 (2017).

[19] S. Hart, Z. Cui, G. Ménard, M. Deng, A. E. Antipov, R. M. Lutchyn, P. Krogstrup, C. M. Marcus, and K. A. Moler, Current-phase relations of InAs nanowire Josephson junctions: From interacting to multimode regimes, Phys. Rev. B **100**, 064523 (2019).

[20] A. Blais, R.-S. Huang, A. Wallraff, S. M. Girvin, and R. J. Schoelkopf, Cavity quantum electrodynamics for superconducting electrical circuits: An architecture for quantum computation, Phys. Rev. A **69**, 062320 (2004).

[21] C. Padurariu and Y. V. Nazarov, Theoretical proposal for superconducting spin qubits, Phys. Rev. B **81**, 144519 (2010).

[22] S. Csonka, L. Hofstetter, F. Freitag, S. Oberholzer, C. Schönenberger, T. S. Jespersen, M. Aagesen, and J. Nygård, Giant fluctuations and gate control of the g-factor in InAs nanowire quantum dots, Nano Lett. **8**, 3932 (2008).

[23] A. A. Kiselev, E. L. Ivchenko, and U. Rössler, Electron g factor in one- and zero-dimensional semiconductor nanostructures, Phys. Rev. B. **58**, 16353 (1998).

[24] M. D. Schroer, K. D. Petersson, M. Jung, and J. R. Petta, Field tuning the g factor in InAs nanowire double quantum dots, Phys. Rev. Lett. **107**, 176811 (2011).

[25] G. W. Winkler, D. Varjas, R. Skolasinski, A. A. Soluyanov, M. Troyer, and M. Wimmer, Orbital contributions to the electron g factor in semiconductor nanowires, Phys. Rev. Lett. **119**, 037701 (2017).

[26] K. Serniak, S. Diamond, M. Hays, V. Fatemi, S. Shankar, L. Frunzio, R. J. Schoelkopf, and M. H. Devoret, Direct dispersive monitoring of charge parity in offset-charge-sensitive transmons, Phys. Rev. Applied **12**, 014052 (2019).

[27] W. Uilhoorn, J. G. Kroll, A. Bargerbos, S. D. Nabi, C.-K. Yang, P. Krogstrup, L. P. Kouwenhoven, A. Kou, and G. de Lange, Quasiparticle trapping by orbital effect in a hybrid superconducting-semiconducting circuit, arXiv e-prints (2021), arXiv:2105.11038.